Monitoring excited state dynamics in cis-[Ru(bpy)2(py)2]2+ by ultrafast synchrotron techniques

Monitoring excited state dynamics in *cis*-$[Ru(bpy)_2(py)_2]^{2+}$ by ultrafast synchrotron techniques

Elisa Borfecchia[a,*], Claudio Garino[a], Diego Gianolio[b], Luca Salassa[c], Roberto Gobetto[a], Carlo Lamberti[a,d]

[a] Department of Chemistry NIS Centre of Excellence and INSTM Reference Center, University of Turin, via P. Giuria 7, 10125 Turin, Italy, e-mail: elisa.borfecchia@unito.it

[b] Diamond Light Source Ltd., Harwell Science & Innovation Campus, Didcot, OX11 0DE Oxfordshire, United Kingdom

[c] CIC biomaGUNE, PaseoMiramón 182, 20009 Donostia, San Sebastián, Spain

[d] CrisDI center of crystallography University of Turin

Abstract

Photoactive metal complexes are applied in a variety of fields, including solar energy conversion, catalysis and medicinal chemistry. Their effectiveness depends on the excited-state features that control the nature of photoreaction intermediates and photoproducts. For this reason, the structural determination of light-induced transient species is fundamental for a rational design of novel photoactive metal complexes. Among the available time-resolved methods, synchrotron-based techniques are emerging as successful tools in detecting ultrafast structural changes in molecules. The aim of this contribution is to review the results obtained by our group combining TR-XSS (Time-Resolved X-ray Solution Scattering) and TR-XAS (Time-Resolved X-ray Absorption Spectroscopy) to study the excited state dynamics in *cis*-$[Ru(bpy)_2(py)_2]Cl_2$, a model compound for ligand releasing applications. Besides a comprehensive summary of our previous work, we report here new findings we obtained by analysis of 100 ps-resolution TR-XSS dataset. The potential of these techniques towards applications in catalysis are discussed in comparison to other time resolved spectroscopies.

Keywords

Metal complexes; photochemistry; synchrotron ultrafast techniques; Time-resolved XAS; Time-resolved X-ray solution scattering; DFT.

1 Introduction

The unique photophysical and photochemical properties of transition metal complexes have been extensively employed in the development of photoactive systems and devices. The number of available electronic excited states (ES), their rich dynamics and the variety of relaxation pathways to the ground state (GS) shown by these coordination compounds allow tuning of their response to light excitation for a wide range of technological applications. Among the most relevant applications, it is worth mentioning solar energy conversion, e.g. in dye-sensitized solar cells (DSSCs) [1-3], photoactivatable antitumoral drugs [4-13], drug delivery systems [14-17], cell-imaging luminescent probes [18, 19], light activated molecular machines [20, 21], light emitters such as organic light emitting diodes (OLEDs) [22-25], and sensors [26].

The activation of transition-metal complexes by visible and UV light considerably enlarges the scope of catalytic transformations. Various elementary steps of catalytic processes, such as generation of coordinatively unsaturated species, ligand exchange, electron transfer, rearrangement reactions and ligand-centred reactivity, can be selectively promoted in such a way. Among these processes, ligand exchange and electron transfer are particularly relevant for catalysis. Such reactions also occur at the ground state, but are strongly affected by electronic excitation [27]. In the literature several examples of reactions photocatalysed with organometallic complexes are reported: cyclizations of alkynes and polyunsaturated substrates, olefin metathesis, migration of double bonds in alkenes and carbonyl insertion, activation of stable C–H bonds in aromatic compounds or alkanes. A large number of publications is focused on photochemical electron-transfer-induced reactions with coordination compounds: photoredox catalysis with ruthenium polypyridyls, cobalt complex-mediated radical reactions, and palladium-catalyzed CO insertion in radical reactions [27,

28]. Moreover, recent developments in artificial photosynthesis highlighted the role of metal photocatalysts in light-driven water splitting and in photocatalytic CO_2 reduction [5, 28-31].

1.1 Accessing structural information on the ultrafast scale: the role of synchrotron-based X-ray methods

Detailed information on the ES dynamics and on the related photochemistry is therefore fundamental for a rational design of novel photoactive metal complexes, of relevance in the aforementioned research areas. A full comprehension of the role played by different ESs in light-induced electronic transitions can guide the introduction of advantageous changes on model molecules. Obtaining experimental structural insights on light-generated transient species is still a challenging and crucial target, also with a view to the validation of computational methods. To achieve such information, the conventional paradigm of time-averaged characterization of the initial and final reaction states has to be replaced with a time-resolved strategy and a time-resolution on the ultrafast timescale (100 fs–few ns) is required to capture the key molecular events triggered by light excitation.

On these bases, the laser pump/laser probe strategy pioneered by Zewail [32-36], in the early 80s, became the principal paradigm in ultrafast time resolved characterization, opening a completely unexplored research field [37, 38]. The conceptual scheme is rather simple: the absorption of a laser pulse triggers the process of interest (pump pulse), subsequently another pulse (probe pulse) records the sample response as a function of the elapsing time-delay [39-43]; time resolution is thus limited only by the longer pulse duration [44, 45].

Optical and vibrational laser pump/laser probe spectroscopies [46, 47] substantially contributed in elucidating the ES dynamics in a multitude of cases [44, 48-61], representing essential tools to elucidate photoreaction kinetics (*vide infra*, Section 2.2.2). However, a direct monitoring of the structural dynamics can be exclusively obtained turning to electrons [62-66] or to X-rays [45, 67-69] probe pulses. In the ultrafast structural X-ray science [45, 67-69], a key-role is played by the properties of third generation synchrotron sources, particularly in term of brilliance, stability, tunability and time-structure of the emission. These capabilities made possible the investigation of the structure of the matter at a level not imaginable before [70-73]. When using laser pump/X-ray probe setups at synchrotrons, the time-resolution is given by the X-rays probe pulse duration: the lowest bunch lengths obtained in third generation machines are in the 30–100 ps interval [67, 74] in normal operation modes of the source. Nevertheless, advanced strategies are emerging to further reduce the duration of X-ray probe pulses from synchrotrons. For instance, the time-resolution can be improved down to few ps to the expenses of flux by operating the source in the so called low-α mode [75-78], where the "momentum compaction factor" α is controlled by the transverse beam optics [79, 80]. Furthermore specially-designed experimental arrangements such as the electron bunch slicing scheme are able to lower time-resolution to few hundreds of fs [81-84].

The time resolution on the 100 ps scale achieved in conventional operation modes allowed to probe thermally equilibrated excited-state structures in a variety of systems [45, 67-69, 85], ranging from small elementary molecules to large biomolecules. With respect to applications in biochemistry/medicine and homogeneous catalysis, an emphasis should be put on the investigation of photoinduced dynamics of the solution phase. Here, several studies employed two highly complementary time-resolved X-ray techniques, namely time-resolved X-ray solution scattering (TR-XSS) [68, 69, 86] and time-resolved X-ray absorption spectroscopy (TR-XAS) [45, 67, 85], to obtained detailed insights on excited state dynamics and geometry in solvated transition metal complexes.

Among the most relevant applications, TR-XSS investigation of the photo-induced rearrangements in the $Ru_3(CO)_{12}$ triangular cluster by Kong *et al.* [87, 88] well demonstrates the potentiality of combining X-ray ultrafast techniques and transient IR spectroscopy. It is worth noting that this Ru-carbonyl cluster has shown photocatalytic activity, inducing selective bonds breaking as a function of the excitation wavelength [89, 90]. TR-XSS also contributed to unravel the ES geometry in two structurally-related photoactive binuclear metal complexes, namely tetrakis-μ-pyrophosphitodiplatinate ($[Pt_2(P_2O_5H_2)_4]^{4-}$, Pt-POP) [91] and $[Ir_2(dimen)_4]^{2+}$, where dimen = 1,8-diisocyano-*p*-menthane [92]. These binuclear complexes show a rich photochemistry [93-

95] and are particularly suitable to be investigated by TR-XSS, due to the high scattering power ensured by the metal-metal atomic pairs. On both dimeric complexes, TR-XSS pointed out significant differences between ES geometries observed in the solution phase with respect to those previously detected in solid state studies, thus emphasizing the need for specific analytic tools and protocols for the investigation of light-induced dynamics directly in solution.

Relevantly to the present work, several recent TR-XAS applications are focused on the ultrafast structural and electronic characterization of transition metal complexes and clusters, often in the solution phase. For instance, Chen and co-workers thoroughly investigated the photoinduced structural dynamics and the ligation mechanisms in different metalloporphyrines, including NiTPP-L_2 and NiTMP (where TPP = nickel tetraphenylporphyrin, L = piperidine and TMP = tetramesitylporphyrin) [96, 97]. In addition TR-XAS was employed to elucidate the MLCT state structure of $[Cu(dmp)]^{2+}$ in acetonitrile (dmp 2,9-dimethyl-1,10-phenanthroline) [53, 98, 99] and the structural modifications promoted by photoinduced intramolecular electron-transfer in $[Ru(bpy)_3]^{2+}$ (where bpy = 2,2′-bipyridine) [100, 101] and in a series of $[ReX(CO)_3(bpy)]^{n+}$ complexes, where X = 4-ethylpyridine (n = 1), Cl, or Br (n = 0) [102].

Furthermore, the technique was employed to investigate the structural distortions in the triplet ESs of binuclear metal complexes, such as the Pt-POP system [103], and the $[Pt(ppy)(\mu\text{-}^tBu_2pz)]_2$ (ppy = 2-phenylpyridine; $^tBu_2pz$ = 3,5-di-tert-butylpyrazolate) complex [104]. Harpham *et al.* [105] combined ps-TR-XAS, transient IR spectroscopy, DFT calculations, and conventional laboratory characterization to investigate the photochemistry of the $[Ru_2(Cp)_2(CO)_4]$ complex (Cp = cyclopentadienyl), proposed as a promising candidate to develop rechargeable "solar batteries" based on photochromic molecules undergoing reversible photoisomerization. Very recently, the same research group employed TR-XAS also to characterize the transient electronic and nuclear configurations in the $Ru_3(CO)_{12}$ cluster [106], previously studied by TR-XSS [87, 88]. Finally, TR-XAS was extensively employed to monitor ultrafast spin crossover in iron complexes, unveiling the structures of elusive high-spin states and clarifying the full photocycle [84, 107-110]. Interestingly, a recent study by Hardlup *et al.* [111] focused on the investigation of the photoinduced low spin to high spin conversion of $[Fe(bpy)_3]^{2+}$ in aqueous solution using a laser pump/X-ray probe synchrotron setup permitting simultaneous TR-XSS and TR-XAS collection at a 3.26 MHz repetition rate.

In this contribution we aim to show the potentialities of these synchrotron ultrafast techniques by describing and discussing the most prominent findings from our recent work [112, 113]. In particular hereafter, we will summarize the results we obtained in different TR-XSS and TR-XAS experiments (performed at the ESRF and APS synchrotrons), integrating the discussion with new insights.

1.2 The cis-$[Ru(bpy)_2(py)_2]^{2+}$ complex: a challenging model system

The complex *cis*-$[Ru(bpy)_2(py)_2]^{2+}$ (where bpy = 2,2′-bipyridine and py = pyridine) can be considered as a prototypic compound to study ligand release and photosubstitution. In this complex, UV and visible excitation in water solution promotes the dissociation of one py ligand with high yield (ca. 20%) [114]. The dissociation is followed by coordination of a solvent molecule, resulting in the *cis*-$[Ru(bpy)_2(py)(H_2O)]^{2+}$ photoproduct (PHP). In terms of ESs dynamics, the efficient py release likely occurs *via* a dissociative metal-centred (^{3}MC) triplet ES. Experimental and computational studies identified the ^{3}MC as the lowest-lying triplet excited state in *cis*-$[Ru(bpy)_2(py)_2]^{2+}$, irreversibly populated through a ^{3}MLCT-^{3}MC potential energy surface crossing (MLCT = metal to ligand charge transfer) [115-120]. The resulting photochemical scenario for aqueous *cis*-$[Ru(bpy)_2(py)_2]Cl_2$ is schematically represented in Fig. 1, with the principal steps of the photoprocess summarized in the reactions (i)–(v'). The simplified Perrin-Jabłoński diagram (Fig. 1b) highlights the hypothesized ES dynamics yielding to PHP upon light-excitation of the GS, reporting the dominant photochemical pathways and the related rate constants k_i.

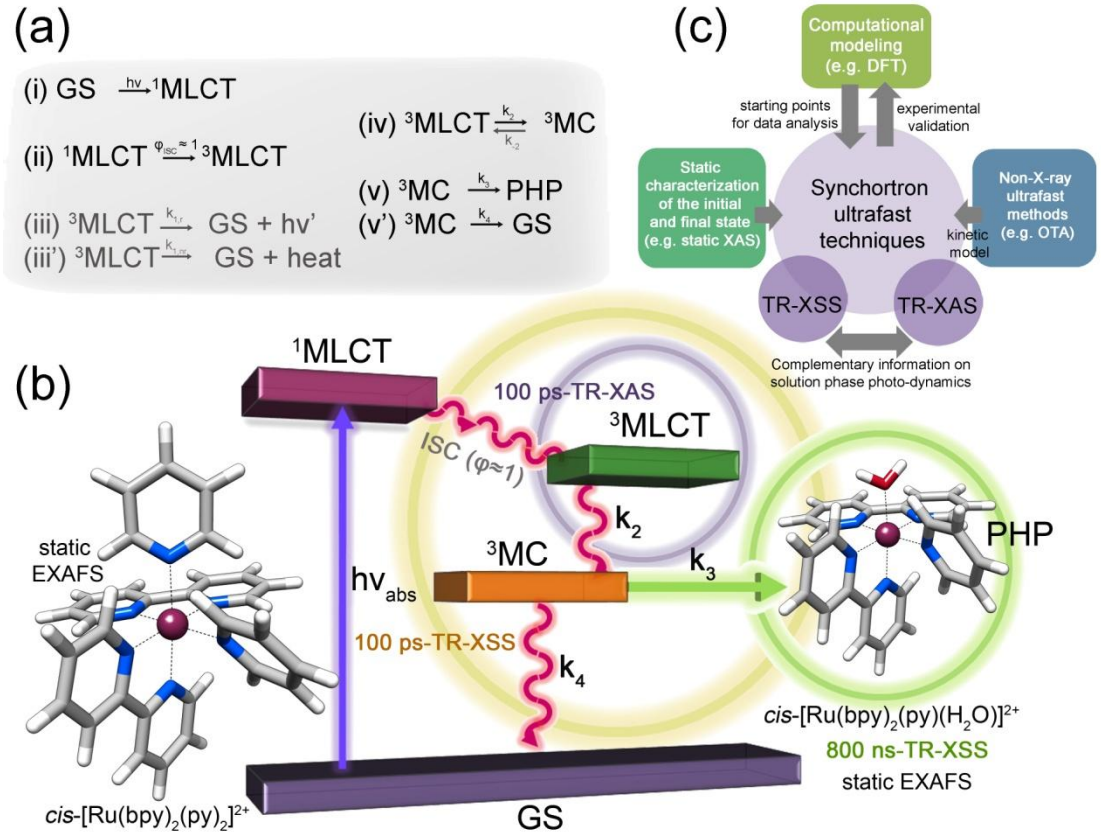

Fig. 1. Photochemical scenario for aqueous *cis*-$[Ru(bpy)_2(py)_2]Cl_2$ upon UV/visible light-excitation. (a) Principal steps of the photoprocess, summarized in reactions (i)–(v'); the principal photochemical pathways are shown in black colour, while minor processes are reported in grey. (b) Simplified Perrin-Jabłoński diagram of the proposed ES dynamics yielding to PHP formation upon light-excitation of the GS complex, with the geometries of the initial (GS) and final (PHP) state of the process. TR-XSS/XAS ultrafast studies which will be discussed in this contribution are indicated, with coloured circles highlighting the specific time-range analysed in each experiment. Parallel methods that we employed to complement and extend the insights from ultrafast X-ray characterization are shown as well (static XAS, Optical Transient Absorption, OTA, and DFT/TD-DFT calculations). (c) Scheme of the methodology applied to experimentally elucidate the solution phase ES dynamics and photochemistry of *cis*-$[Ru(bpy)_2(py)_2]Cl_2$.

Notably, computational analysis supported the understanding of the photochemistry of *cis*-$[Ru(bpy)_2(py)_2]^{2+}$ and similar complexes [121, 122], however obtaining experimental structural information on transient species generated by light excitation remains crucial. It is worth noting that, despite its simple structure, this system represents a challenge for time-resolved X-ray techniques, due to the irreversible nature of the photoreaction, involving the release of a multi-atomic fragment constituted by weakly scattering low-*Z* atoms. In addition, multiple species are simultaneously present in the laser-excited volume, with geometry slightly different one from each others. Furthermore, *cis*-$[Ru(bpy)_2(py)_2]^{2+}$ is suited to test synchrotron pump-and-probe techniques, defining optimized experimental strategies and data analysis protocols, towards more sophisticated (e.g. in biologically- or catalytically-relevant) applications of these novel characterization tools.

To address this inherent complexity, we developed the integrated methodology schemed in Fig. 1c. The core of the characterization strategy is represented by the TR-XSS and TR-XAS techniques. This *duo* brilliantly conjugates the global view provided by the solution scattering method (solute rearrangements but also solvent-related dynamics) with the XAS elemental selectivity, allowing an enhanced sensitivity around the metal centre. Crucially, the interpretation of the TR-XSS and TR-XAS data has been assisted and complemented by DFT-based modelling, by a thorough static XAS characterization of the initial (GS) and final (PHP) steps of the photoreaction and by OTA experiments to clarify the kinetics of the process, allowing a more stable fit of the TR-XAS data.

2 Synchrotron ultrafast techniques to monitor photoactive metal complexes: the case of *cis*-$[Ru(bpy)_2(py)_2]^{2+}$

2.1 TR-XSS

2.1.1 Data acquisition and reduction strategy to isolate the solute-related contribution to TR-XSS signal

The TR-XSS technique relies on the acquisition of the X-ray scattering signature of the solution both after the absorption of the laser pump pulse ($\tau > 0$) and before the excitation ($\tau_0 < 0$). The experimental setup employed to perform TR-XSS measurements at the ID09b beamline of the ESRF is shown in Fig. 2a, and concisely described in the Supporting Information, whereas a detailed technical description can be found elsewhere [68, 69, 73, 123]. As shown in Fig. 2b, the I(q, τ = 800 ns) and I(q, τ_0 = – 2000 ns) curves collected for a 20 mM aqueous solution of *cis*-$[Ru(bpy)_2(py)_2]Cl_2$ are substantially equivalent. Indeed, a critical point in TR-XSS experiments is the smallness of the photoinduced signal, at least at typical working concentrations in the 1 mM – 50 mM range. The rearrangements occurring upon laser excitation in the solution can be however enhanced by calculating the differential scattered intensity $\Delta I(q, \tau) = I(q, \tau) - I(q, \tau_0)$. The corresponding $\Delta I(q, \tau = 800$ ns) is plotted for comparison on the right ordinate axis of Fig. 2b. It can be noticed that a well structured signal emerges, although extremely reduced in intensity when compared to the not differential scattering signal ($\Delta I(q, \tau) / I(q, \tau) \sim 10^{-3}$). Dealing with a so reduced signal, a huge statistics of acquisition in the most stable experimental conditions is sorely needed for structural analysis. The remarkable improvement in data quality observed e.g. after acquiring ~ 500 pairs of laser off/laser on CCD images for each time delay and averaging the corresponding $\Delta I(q, \tau)$ is illustrated in Fig. 2b.

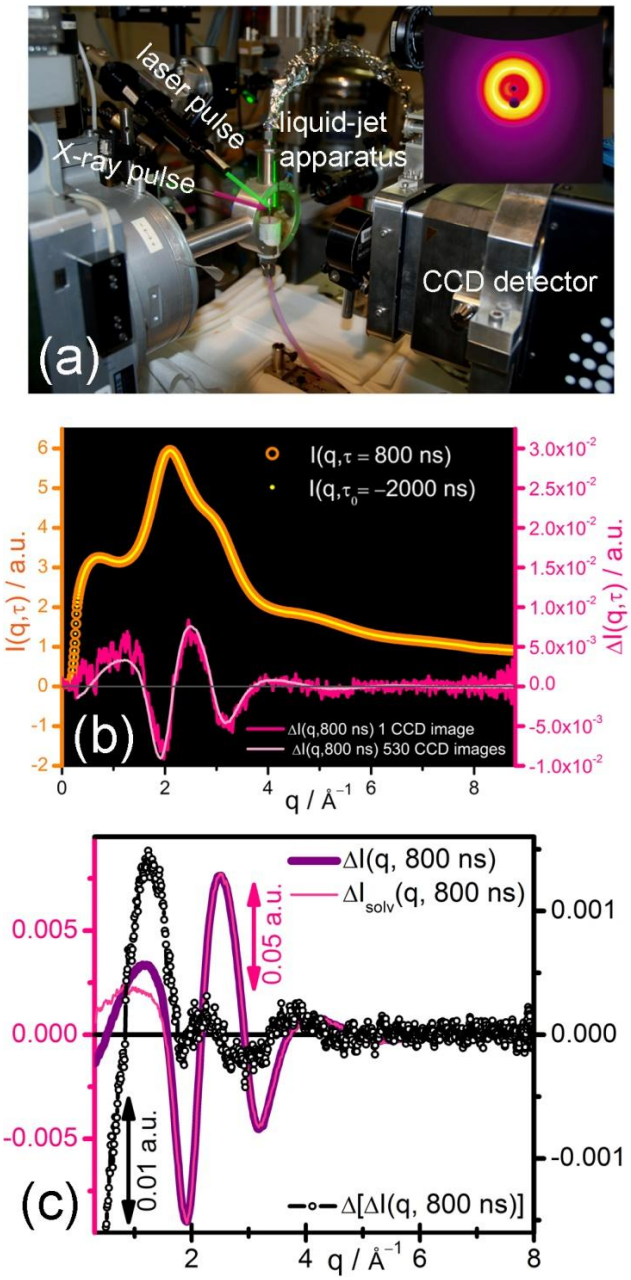

Fig. 2. (a) Photograph of the experimental setup for TR-XSS measurements at the ID09B beamline, showing the liquid jet apparatus, the experimental arrangement around the interaction point between the jet and the laser pump/X-ray probe pulses and the FReLoN CCD detector. The inset reports a typical corrected CCD image acquired for a 20 mM aqueous solution of *cis*-$[Ru(bpy)_2(py)_2]Cl_2$. (b) Left ordinate axis (in orange): superimposition of I(q, τ = 800 ns) and I(q, τ_0 = –2000 ns) curves (open orange circles and yellow dots, respectively). Right ordinate axis (in purple): difference signal $\Delta I(q, \tau = 800\ ns) = I(q, \tau = 800\ ns) - I(q, \tau_0 = -2000\ ns)$, from an individual pair of CCD acquisitions (pink noisy curve) and after averaging ~ 500 pairs of laser off/laser on CCD images (light pink curve). It is worth noting that the low-q region of the $\Delta I(q, \tau)$ curves is strongly sensitive to possible instabilities in the liquid jet: this can cause a discrepancy out of the noise level between some individual scans and the high-statistics average curve. (c) Left ordinate axis (in pink): comparison between the $\Delta I(q, \tau = 800\ ns)$ reported in part (b) (thicker purple curve) and the scaled $\Delta I_{solv}(q, \tau)$ curve (thinner pink line), obtained repeating the TR-XSS experiment using $KMnO_4$ as photochemically inert solute. Right ordinate axis (in black): solute-related contribution $\Delta[\Delta I(q)]$, isolated after the subtraction of the $\Delta I_{solv}(q, \tau)$ term: $\Delta[\Delta I(q)] = \Delta I(q) - \Delta I_{solv}(q)$. The application of the NIR-method in the 100-ps-resolution experiment yielded comparable results. Unpublished Figure, reporting data originally published in ref. [112].

The XSS technique, as all diffraction-based methods, is not elementally selective and provides information on the arrangement of all the atoms in the volume probed by the X-ray pulses. In particular, the differential TR-XSS signal $\Delta I(q, \tau)$ contains time-dependent contributions due to the changes in solute-solute, solute-

solvent (cage) and purely-solvent terms. As commonly observed in TR-XSS experiments [73], all the $\Delta I(q, \tau)$ curves collected for *cis*-$[Ru(bpy)_2(py)_2]Cl_2$ in water are dominated by the purely-solvent contribution $\Delta I(q, \tau)_{solv}$, due to the rearrangement in the solvent bulk structure upon ultrafast heat-release from the laser-excited solutes [68, 69] (see Fig. 2c). The investigation of the solvent-related dynamics and of the solute-solvent interplay is fundamental for a thorough comprehension of solution-phase photochemistry of metal complexes [124]. This information can be preferentially obtained with the TR-XSS technique. However, when specifically interested to photoinduced structural modification in the metal complex (solute-solute and cage contributions to experimental $\Delta I(q, \tau)$ curves), a reliable modelling of the $\Delta I(q, \tau)_{solv}$ term is required. In particular, we employed the inert solute method [73, 92, 112] in the analysis of the 800 ns-resolution dataset. Conversely, for the analysis of 100 ps-data the solvent-only thermodynamic contribution was determined by performing a blank heating experiment on pure water [68, 125] which ensures a more accurate modelling of the experimental signal in particular at the shorter time-scales. Here, the solvent is vibrationally excited with near-infrared ultrafast laser pulses (at 1458 nm in our experiment) and the structural modifications in water bulk structure following hydrodynamic relaxation are probed by 100 ps X-ray pulses from the synchrotron.
Once the $\Delta I_{solv}(q)$ curve has been experimentally obtained and properly scaled to the global differential scattering signal, it can be subtracted to isolate the solute-related contribution, namely $\Delta[\Delta I(q)] = \Delta I(q) - \Delta I_{solv}(q)$. The $\Delta[\Delta I(q, \tau = 800\ ns)]$ curve obtained for *cis*-$[Ru(bpy)_2(py)_2]^{2+}$ is reported as an example in Fig. 2c [112]. These time-dependent curves represent the final datum in q-space after the data reduction procedure summarized so far. A more intuitive interpretation of the differential curves can be obtained moving from q-space to real distances r-space, which are bridged by a sine-Fourier transform operation [68, 126]. Real space TR-XSS signals, hereinafter referred to as $\Delta[\Delta I(r, \tau)]$, are directly related to the variation in the atom-atom pair distribution function from the laser on to the laser off states [127-130]. Here, when monitoring ligand photo-substitution, positive and negative peaks identify bond formation and cleavage at interatomic distances corresponding to the r-position of the maxima and minima of the $\Delta[\Delta I(r, \tau)]$. Furthermore, the simulation of the TR-XSS signal, e.g. from suitable DFT-optimized geometries of chemically meaningful intermediates, can fingerprint the molecular distortions occurring in the ESs accessed upon light-excitation.

2.1.2 Insights in pyridine photosubstitution and excited state dynamics of *cis*-$[Ru(bpy)_2(py)_2]^{2+}$ using TR-XSS

The insights we achieved using TR-XSS to monitor the light-induced structural dynamics of *cis*-$[Ru(bpy)_2(py)_2]^{2+}$ are summarized in Fig. 3. These results were obtained in two subsequent experiments, improving the time-resolution from the quasi-static 800 ns case to the more recent 100-ps study. Let us first summarize the results on the final state of the photoreaction, safely identified by data collection up to 5 μs after excitation, which does not show any appreciable time-evolution of the TR-XSS features [112]. The experimental $\Delta[\Delta I(r, \tau = 800\ ns)]$ is reported in Fig. 3a after scaling of the experimental differential intensity to absolute scattering units, see Supporting Information. The curve is characterized by a negative shoulder at ~ 2.5 Å, whereas two well-defined negative peaks are observed at ~ 3.1 and ~ 4.7 Å. The presence of these negative features is consistent with the dissociation of one py unit from the metal centre. Indeed, the r-positions of the three minima are in good qualitative agreement with the distances of the nitrogen atom and of the two pairs of *para*- and *meta*-carbon atoms of the py ring from the ruthenium centre, according to the DFT-optimized geometry of the GS complex. It is worth noting that the DFT-geometry of the GS structure of *cis*-$[Ru(bpy)_2(py)_2]^{2+}$ has been independently validated using static XAS data collected at the ESRF [112] and at the APS [113, 131]. The use of the DFT structure in the fitting of the EXAFS data yielded very good results, although the EXAFS bond distances showed a systematic shortening (0.02–0.04 Å) with respect to the computed ones.
A more robust interpretation of the data was achieved on the basis of TR-XSS simulated curves, calculated in the framework of a simplified scattering model employing DFT-optimized structures of the GS and three candidate structures for the final states of the photoprocess (Fig. 3d, P_1–P_3 structures). The model P_1 only accounts for py dissociation, P_2 includes the coordination of a solvent molecule to form a PHP such as

$[Ru(bpy)_2(py)(H_2O)]^{2+}$. Finally in P_3, the PHP structure is optimized by adding a small cage of three water molecules, H-bonded to the H_2O ligand directly coordinated to the Ru centre. P_3 roughly models, at the gas-phase level, the rearrangement of the water cage structure around the $[Ru(bpy)_2(py)(H_2O)]^{2+}$ PHP.

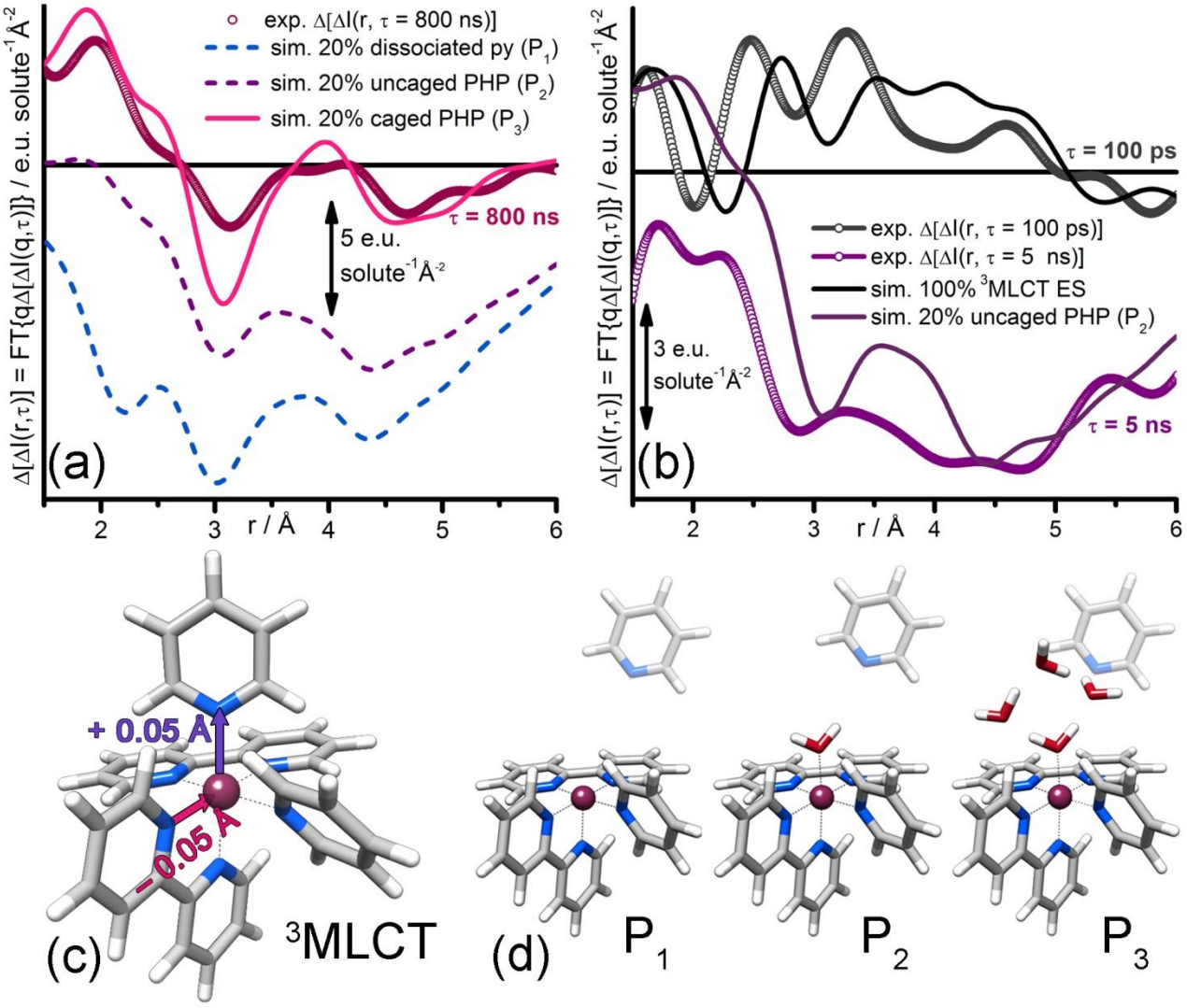

Fig. 3. (a) Results from 800-ns resolution TR-XSS experiment. The experimental $\Delta[\Delta I(r, \tau = 800\ ns)]$ (dark pink circles) is compared to three simulated TR-XSS curves, calculated from the DFT-optimized structures of the GS and the three candidate structures for the final states of the photoprocess (considering a 20% dissociation yield), namely P1–P3, shown in part (d). (b) Selection of results from the improved 100-ps resolution TR-XSS experiment and preliminary interpretation. The experimental $\Delta[\Delta I(r, \tau)]$ curves measured for τ =100 ps (gray circles) and τ = 5 ns (purple circles) are reported. 100 ps-data are compatible with the TR-XSS simulated curve calculated from the DFT-optimized structure of the ^{3}MLCT ESs shown in part (c) (solid black line), while the $\Delta[\Delta I(r, \tau = 5\ ns)]$ curve is satisfactorily reproduced by the simulation obtained from the uncaged PHP model (P_2). (c) DFT-optimized geometry of the ^{3}MLCT ES of *cis*-$[Ru(bpy)_2(py)_2]^{2+}$; the major distortions with respect to the GS geometry are highlighted by coloured arrows. (d) DFT-optimized structures of the three possible final states of the photoprocess tested: P_1 (py dissociation), P_2 (uncaged PHP, i.e. py dissociation and water coordination) and P_3 (caged PHP, where a small cage of three water molecules has been added and optimized). Unpublished Figure; part (a) reports data originally published in ref. [112], scaled in e.u. solute^{-1} Å^{-2}.

The scaling of TR-XSS data to an absolute scattering scale allows a quantitative evaluation of the concentration of the PHP species tested as possible candidates for the final step of the photoreaction. Watching, in a quasi-static fashion, the end point of the photo-process (as demonstrated by the equivalence of all TR-XSS curves collected for $\tau \geq 800$ ns, up to 5 μs), we can safely assume that any direct structural contributions from ES species is already ceased. Furthermore, for the sake of quantitative analysis, we can

refer to previous studies reporting a dissociation yield φ = 0.2 for the complex of interest [114, 132]. On these bases, we obtained the simulated curves reported in Fig. 3a, calculated by Fourier transforming the differential scattering intensity 0.2 $\Delta I_{Pi}(q)$ = 0.2 [$I(q)_{Pi}$ –$I(q)_{GS}$], where $I(q)_{Pi}$ (i = 1–3) is the scattered intensity calculated for each of the geometries P_1–P_3 using the Debye equation [133-135], $I(q)_{GS}$ is the scattered intensity computed for the structure of the GS complex, and the factor 0.2 accounts for the dissociation yield φ.

Passing from the model P_1 to P_2 (Fig. 3a), a progressively better reproduction of the experimental Δ[ΔI(r, τ = 800 ns)] is observed, in particular for the shoulder-like feature at ~ 2.5 Å. The introduction of the small water cage in P_3 (Fig. 3a) remarkably improves the agreement between the simulated and the experimental curve. Indeed, the additional electron density associated to the water cage, which likely approaches the metal centre after the py release, partially balances the negative contribution due to ligand dissociation.

The improved 100 ps-resolution of our more recent TR-XSS study allowed to confirm these results and to directly monitor the earlier dynamics of the photoprocess. These findings are also in good agreement with the picture emerging from TR-XAS and OTA characterization, reviewed in Section 2.2. A selection of the collected experimental data is reported in Fig. 3b, including the Δ[ΔI(r, τ)] curves for τ = 100 ps and 5 ns, shown as grey and purple circles respectively. Although we are currently working to refine the structural interpretation of these data, the preliminary simulations reported in Fig. 3b clearly highlights how the py photodissociation occurs on the few ns-timescale. In particular, the Δ[ΔI(r, τ = 100 ps)] curve is compatible with the differential scattering computed from the DFT-optimized geometry of the ^{3}MLCT ES of *cis*-$[Ru(bpy)_2(py)_2]^{2+}$ (Fig. 3c), assuming 100% population of the ES. Here, the major distortions with respect to the GS geometry are a ~ 0.05 Å rigid lengthening of the bond length of one py ligand from the metal centre and a ~ 0.05 Å contraction along the Ru–N bond axis for the ring of the bpy ligand in *trans* position to the distanced py. From qualitative comparison between the Δ[ΔI(r, τ = 100 ps)] data and the ^{3}MLCT simulated curve (Fig. 3c), it can be noticed that the highly structured experimental signal is satisfactorily reproduced, although its features are systematically shifted to slightly shorter r-values with respect to the simulation. This inconsistency can be related to the above mentioned DFT tendency to overestimate the Ru–N(ligands) bond lengths in polypyridyl Ru-complexes [122]. Further analysis will include a testing of slightly modified ^{3}MLCT guess geometries, obtained by systematic variation of the key-bond lengths, and a searching for the best fit to the Δ[ΔI(r, τ = 100 ps)] curve. However, due to the lack of element-selectivity, a lower sensitivity of the TR-XSS technique (e.g. with respect to TR-XAS) to the very small structural rearrangement in the ligands positions around the metal centre is expected. Conversely, the TR-XSS technique is particularly suited to clarify the longer-distance rearrangements in the solvation shell, which are scarcely detectable using the local XAS-based methods. In particular, the Δ[ΔI(r, τ = 5 ns)] curve reported in Fig. 3b is consistent with the uncaged PHP structure (model P_2), as demonstrated by the related simulation (Fig. 3b). It is worth noting that the TR-XSS data that we collected after 100 ns were substantially equivalent to the Δ[ΔI(r, τ = 800 ns)] curve reported in Fig. 3a, thus suggesting that the rearrangement in the water cage around the newly formed PHP units occurs in the 10–100 ns timescale. We are planning to perform a more sophisticated modelling of the solute-solvent interaction (e.g. *via* MD), to improve the reproduction of experimental data and achieve deeper insight in the solvent-related dynamics, thus exploiting at the best the potentialities of the TR-XSS technique.In conclusion, the 800 ns TR-XSS data are fully compatible with a final state where the 20% of the excited *cis*-$[Ru(bpy)_2(py)_2]^{2+}$ complexes have one py photosubstituted by a water molecule. Furthermore, the better agreement found in correspondence of the caged PHP model P_3 suggests that after 800 ns from excitation the solvation shell has already rearranged, extending towards the Ru centre. The improved TR-XSS collected down to 5 ns from excitation suggests for this cage-rearrangement process a dynamics on the 10–100 ns timescale. Finally, the TR-XSS signal at the earlier delays probed (down to 100 ps) shows a substantial contribution from the ^{3}MLCT ES geometry, confirming the scenario depicted by the TR-XAS and OTA data presented below.

2.2 TR-XAS

2.2.1 XAS characterization of *cis*-$[Ru(bpy)_2(py)_2]^{2+}$: form static to time-resolved structural information

TR-XAS [45, 67, 74] is a perfect tool to experimentally validate the photochemical scenario proposed in Section 2.1 for the model compound *cis*-$[Ru(bpy)_2(py)_2]^{2+}$. Moreover, the TR-XSS and TR-XAS techniques provide highly complementary structural views on solution phase photoreactions. The latter approach is indeed ideal to complement the ultrafast solution scattering results presented in Section 2.1, in particular to elucidate the atomic rearrangements of *cis*-$[Ru(bpy)_2(py)_2]^{2+}$ in its ESs. A reliable interpretation of the transient data is however subjected to a detailed knowledge of the initial and terminal points of the photoprocess, *i.e.* the GS and PHP geometries, primarily accessible using static EXAFS spectroscopy. With this respect, Fig. 4 illustrates the passage from static to time-resolved XAS characterization for *cis*-$[Ru(bpy)_2(py)_2]^{2+}$.

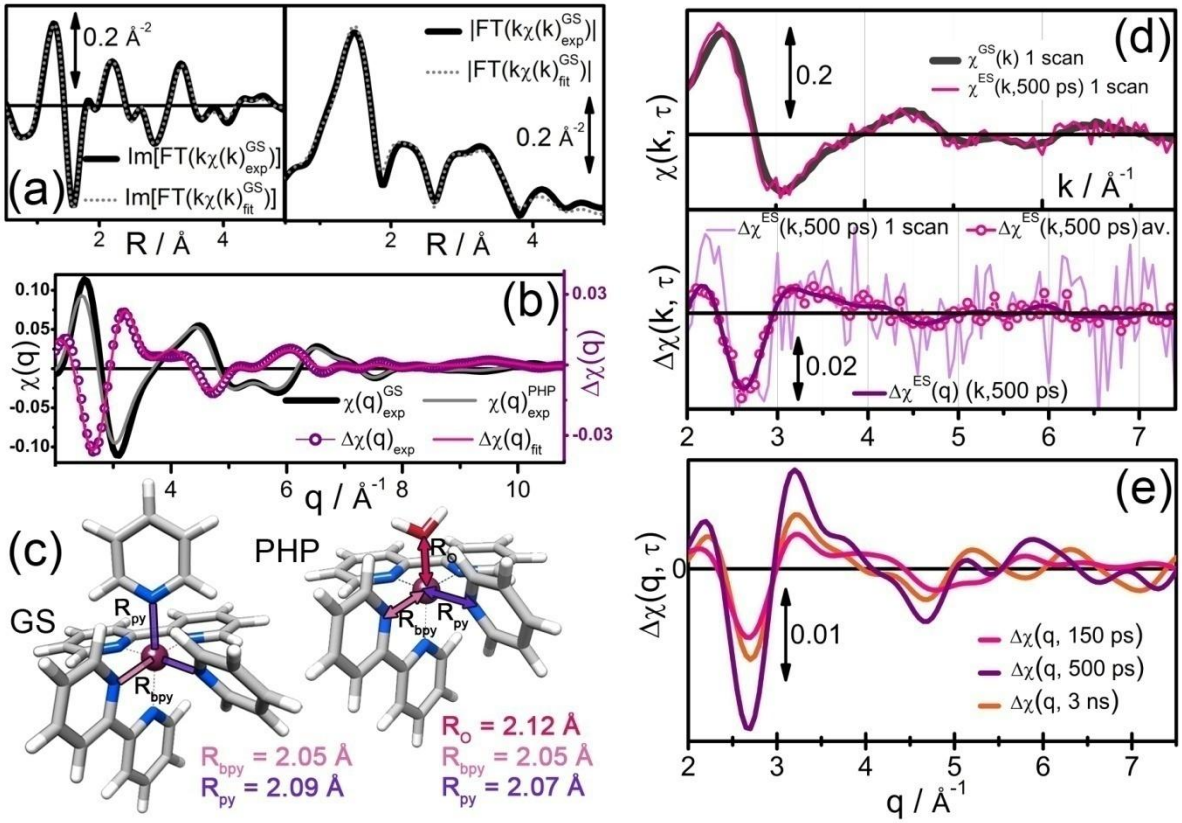

Fig. 4. Summary of EXAFS results from static characterization of the GS and PHP species and extension to the investigation of the ultrafast structural dynamics by TR-EXAFS. (a) Conventional EXAFS fitting of GS spectrum $\chi^{GS}_{exp}(k)$: k-weighted FT functions for the experimental (black thick lines) and best fit curves (grey dotted lines) are reported both for the imaginary part (left panel) and the modulus (right panel). (b) Left ordinate axis (in black): comparison between $\chi^{GS}_{exp}(q)$ for GS and $\chi^{PHP}_{exp}(q)$ for PHP. Right ordinate axis (in purple): experimental differential curve $\Delta\chi^{PHP}_{exp}(q) = \chi^{PHP}_{exp}(q) - \chi^{GS}_{exp}(q)$ (purple circles) and relative best fit (pink solid line) obtained from q-space differential refinement of the EXAFS data. (c) Pictorial representation of the structural parameters optimized by conventional r-space fitting of the GS EXAFS data and by q-space differential fitting of the PHP spectrum. The PHP model is equivalent to the P_2 geometry, employed in the analysis of the TR-XSS data (see Fig. 3 and related discussion) Correspondent best-fit values are reported. (d) TR-EXAFS data acquisition and reduction strategy. Top panel: comparison between a pair of individual $\chi^{GS}(k)$ and $\chi^{ES}(k, 500\ ps)$ spectra collected at the 11-ID-D beamline of the APS, reported as dark grey and pink solid lines, respectively. The $\Delta\chi^{ES}(k, 500\ ps) = \chi^{ES}(k, 500\ ps) - \chi^{GS}(k)$ transient data obtained from the pair of individual scans in top panel (light violet curve) are reported, compared with the $\Delta\chi^{ES}(k, 500$ ps) curve obtained averaging 40 differential scans (pink circles), and the FT-filtered average curve ($\Delta\chi^{ES}(q, 500$ ps), purple solid line, k range 2.5−10.8 Å^{-1} for the forward FT, r-range 1.0−5.0 Å for the backward FT). (e) $\Delta\chi(k, q)$ transient spectra for τ = 150, 500 and 3000ps, reported in pink, purple and orange, respectively. Unpublished Figure; panels (a), (b) and (e) report data from ref. [113].

Initially we obtained an extremely accurate fit of the GS spectrum, as shown in Fig. 4a. A detailed discussion of the fit details can be found in ref. [113], whereas here we will focus on the structural information derived

from the analysis. In particular, the EXAFS paths where parameterized as a function of the Ru−N(bpy) and Ru−N(py) bond distances (namely R_{bpy} and R_{py}), assuming the coordination of the metal centre to rigid ligand units. Optimized values of R_{py} = (2.09 ± 0.03) and R_{bpy} = (2.05 ± 0.02) Å were found, in good agreement with the DFT geometries although slightly shorter, as already pointed out in Section 2.1 (see also Fig. 4c). The comparison between the spectra of GS and PHP remarks how the photochemistry of *cis*-$[Ru(bpy)_2(py)_2]^{2+}$ is a challenge also for the EXAFS technique, despite the simple structure of this metal complex. The $\chi^{GS}{}_{exp}(q)$ and $\chi^{PHP}{}_{exp}(q)$ spectra are plotted in Fig. 4b: their striking similarity reflects the structural analogy between the two species, at least from an EXAFS perspective. Indeed, the first-shell signal is only minimally perturbed upon the N(py) → O(H_2O) photosubstitution. The subsequent coordination shells suffer of the signal loss due to lacking scattering paths which involve the atoms of one py ring in the GS structure. However, the cumulative contribution of such paths can be estimated to be only 1/6 of the global signal.

As expected, a careful analysis revealed that the spectra of the GS and PHP complexes in water solution are hardly distinguishable applying the conventional r-space fitting of Fourier transformed EXAFS data [113, 131]. Similarly to what discussed for TR-XSS data, once a high control on the data acquisition and reduction is achieved, the differential approach is a powerful strategy to enhance the effect of very small structural modifications on the experimental signal. In the field of ultrafast X-ray characterization, the direct fitting of the differential signal in the energy/momentum space is recently imposing as an attractive alternative, ensuring a superior accuracy for the derived structural parameters if compared to conventional r-space fitting methods [103, 136]. The differential fitting strategy relies on the identification of the key parameters to optimize, structural (bond distances) and not (e.g. Debye-Waller (DW) factors and energy shifts for EXAFS refinements). Subsequently, a statistically significant array of differential theoretical spectra, correspondent to systematic variations of these parameters from a reference structure (e.g. the GS geometry), is computed. Finally, the best agreement between the experimental and theoretical differential signals is searched (e.g. *via* R-factor minimization in the N-dimensional space for N simultaneously varied parameters) yielding the best fit curve and correspondently the optimized values of the parameters. We applied this methodology in the fitting of the TR-XAS data (*vide infra*, Section 2.2.2), and also to obtain a more reliable refinement of the PHP structure from the comparison between the static XAS data collected for *cis*-$[Ru(bpy)_2(py)_2]^{2+}$ and *cis*-$[Ru(bpy)_2(py)(H_2O)]^{2+}$ in aqueous solution. Interestingly, this study paves the way to possible applications of such a fitting strategy, so far mainly limited to the analysis of ultrafast X-ray data, in a variety of fields, including catalysis, where the discrimination of closely related structures is a key-target [131].

In this framework, we determined the experimental differential spectrum for the PHP, namely $\Delta\chi^{PHP}{}_{exp}(q) = \chi^{PHP}{}_{exp}(q) - \chi^{GS}{}_{exp}(q)$, shown in Fig. 4b. The differential fitting resulted in the $\Delta\chi^{PHP}{}_{fit}(q)$ curve, superimposed to the experimental differential data in Fig. 4b [113, 131]. On the structural ground, differential analysis mainly indicated a Ru−O(H_2O) bond distance of (2.12 ± 0.01) in the PHP, 0.03 Å longer than the average Ru−N(py) bond length observed using conventional EXAFS analysis of the GS spectrum (Fig. 4c). These results played a key-role in the data modelling of the time resolved experiment, due to the major contribution of the PHP structural component to the total time-dependent differential signal (*vide infra*, Section 2.2.2).

Let us now focus on the 100 ps-resolution TR-XAS measurements performed at the 11ID-D beamline of the APS [97, 98, 104, 137-140]. The challenges tackled in the discrimination between the GS and PHP signals became more and more critical when entering the time-domain. An enhanced acquisition statistics and a differential approach in the data analysis are crucial to unravel the light-driven structural dynamics (see Fig. 4d). In particular, we focused on the analysis of the EXAFS region of the TR-XAS spectrum (TR-EXAFS) for its strong dependency on bond distances, and for the lack of well-defined pre-edge features in the XANES of *cis*-$[Ru(bpy)_2(py)_2]^{2+}$. The average Fourier-filtered $\Delta\chi(q, \tau)$ transient spectra collected for τ = 150, 500 and 3000 ps on a 1 mM *cis*-$[Ru(bpy)_2(py)_2]^{2+}$ aqueous solution excited using 5 ps-long 351 nm laser pulses (see ref [113] and Supporting Information for experimental details) are reported in Fig. 4d. The curves for the three probed delays show a significant time-dependent evolution of the differential features,

especially as regards the intensity of the first differential oscillation and in the position of the minimum at ~ 2.7 $Å^{-1}$. These filtered data selectively contain information on the atomic rearrangements occurring in the 1−5 Å r-space range from the Ru centre, where the physically meaningful photoinduced modifications are expected to occur. The procedure we have applied in their fitting and interpretation, resulting in the elucidation of the major structural features of the longer-lived ^{3}MLCT ES, is summarized in the next Section.

2.2.2 OTA-assisted fitting of the 100 ps-TR-EXAFS data: combining kinetic and structural information to unravel ESs dynamics and geometry

The combination between pump and probe X-ray and optical absorption spectroscopies has been established as an extremely powerful tool to investigate ultrafast light-induced dynamics [45]. Indeed, the two techniques nicely complement each other: the time-evolution of the optical absorption bands which fingerprint the different intermediate species and photoproducts allows for a handier determination of the reaction kinetics, whereas the X-ray probe obviates the OTA lack of direct structural sensitivity. Remarkably, milestone works exploiting this approach, especially by the Chen's group [45] [97], focused on the solution phase photochemistry of transition metal complex, and OTA results were also fundamental in our investigation on *cis*-$[Ru(bpy)_2(py)_2]^{2+}$.

OTA spectra $\Delta A(\lambda, \tau) = A^{ES}(\lambda, \tau) - A^{GS}(\lambda)$, where A denotes the optical absorbance, collected in the 20–2860 ps range for the complex of interest are reported in the inset of Fig. 5a. The negative peak dominating the 450–500 nm wavelength range mainly derives from the GS bleach, although it likely contains unresolved minor contributions from ^{3}MC ES and PHP absorption. In addition, the broad positive signal in the 525–750 nm range can be safely assigned to the ^{3}MLCT ES absorption of $[Ru^{III}(bpy)(bpy^{-})(py)_2]^{2+}$. The main panel of Fig. 5a reports the $\Delta A(\tau)$ curves obtained plotting as a function of the time delay τ the ΔA values reported in the inset for a series of λ-values sampled in correspondence of the major spectral features (GS bleach: λ = 467 nm: pink, λ = 484 nm: purple; ^{3}MLCT ES absorption: λ = 651 nm: blue; λ = 700 nm: light blue; λ = 723 nm: green). Multi-exponential global fits of the $\Delta A(\tau)$ curves highlighted the presence of two major time components, namely τ_1~ 130 ps and τ_2~ 1700 ps.

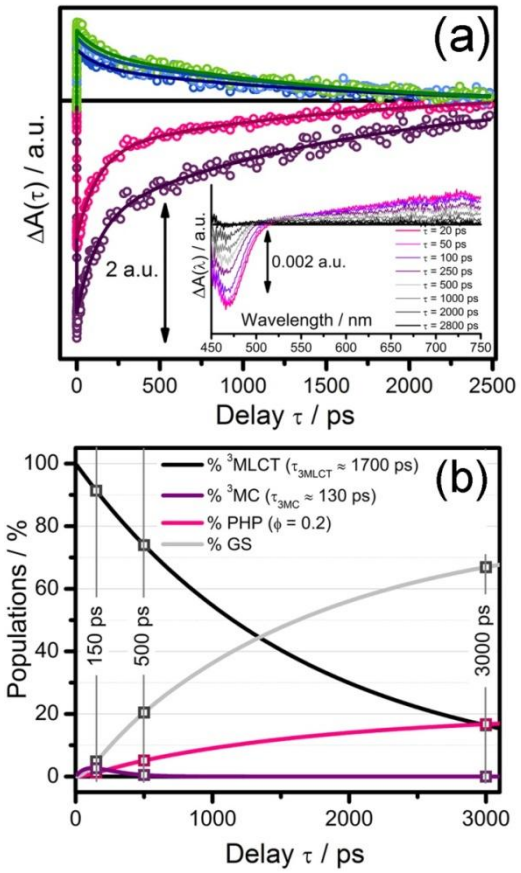

Fig. 5. OTA insights in the ps−ns dynamics of *cis*-$[Ru(bpy)_2(py)_2]^{2+}$ and derived photoreaction kinetics. (a) Inset: OTA spectra ΔA(λ) of *cis*-$[Ru(bpy)_2(py)_2]^{2+}$ in aqueous solution (0.2 mM) collected in the 20–2860 ps range (λ_{exc}= 350 nm) from ref. [113]. Main panel: ΔA(τ) curves (open circles) obtained plotting as a function of the time delay τ the ΔA values reported in the inset for 5 selected λ-values (λ = 467 nm: pink; λ = 484 nm: purple; λ = 651 nm: blue; λ = 700 nm: light blue; λ = 723 nm: green); correspondent bi-exponential global fits (optimized time constants: τ_1 ~ 130 ps and τ_2 ~ 1700 ps) are reported as solid lines. (b) Time evolution of GS, ^{3}MLCT, ^{3}MC populations and PHP percentage calculated according to the photochemical scenario reported in Fig. 1 and employing the time-components identified by OTA (τ_2 ~ 1700 ps = τ_{3MLCT}, τ_1 ~ 130 ps = τ_{3MC}). GS grey solid line; ^{3}MLCT black solid line, ^{3}MC purple solid line, PHP pink solid line. Empty squares and vertical lines are place in correspondence of the time delays monitored using TR-XAS. Adapted with permission from ref. [113]. Copyright RSC (2013).

On the basis of previous studies on *cis*-$[Ru(bpy)_2(py)_2]^{2+}$ and analogues complexes [116, 118, 141, 142], we assigned the OTA decay constants to the lifetimes of the two ESs involved in the photoprocess, *i.e.* ^{3}MLCT and ^{3}MC/photochemistry (see Fig. 1 and related discussion). This assignment is also confirmed by a recent work by Hauser and co-workers [120], where OTA studies evidenced ultrafast quenching of the ^{3}MLCT Luminescence *via* a ^{3}MC state in two ruthenium(II) tris-bipyridyl complexes, namely $[Ru(m\text{-}bpy)_3]^{2+}$ (m-bpy = 6-methyl-2,2′-bipyridine) and $[Ru(tm\text{-}bpy)_3]^{2+}$ (tm-bpy = 4,4′,6,6′-tetramethyl-2′,2′-bipyridine).
Importantly, this allowed to clarify the photoreaction kinetics, and to quantify the time-evolution for the ESs populations and for the PHP percentage, as shown in Fig. 5b. The kinetic information, integrated with the static XAS analysis of the GS and PHP geometries and the computational work, was fundamental to assist the differential fitting procedure of the TR-EXAFS spectra reported in Fig. 4e. Specifically, we identified the PHP and the longer-lived ^{3}MLCT ES as the dominant light-generated species contributing to the differential EXAFS signal at the investigated time points, according to the plots shown in Fig. 5b. Thus we fitted each experimental Δχ(q, τ) curve to theoretical spectra $\Delta\chi_{fit}(q, \tau)$ obtained combining the differential EXAFS signal simulated from PHP and ^{3}MLCT ES geometries, namely $\Delta\chi^{PHP}(q)$ and $\Delta\chi^{3MLCT}(q, R_{py}, R_{bpy})$. The best fit curve is therefore searched as $\Delta\chi_{fit}(q, \tau) = f^{PHP}(\tau)\,\Delta\chi^{PHP}(q) + f^{3MLCT}(\tau)\,\Delta\chi^{3MLCT}(q, R_{py}, R_{bpy})$, optimizing the $f^{PHP}(\tau)$ and $f^{3MLCT}(\tau)$ amplitudes and, on the structural ground, the key structural parameters for the ^{3}MLCT ES, *i.e.* R_{py} and R_{bpy}. Indeed, to model the $\Delta\chi^{PHP}(q)$ contribution we employed the PHP structural

minimum obtained from differential refinement of the static EXAFS data, whereas the ^{3}MLCT geometry has been refined contextually to TR-EXAFS fitting routine. On the basis of the DFT results introduced in Section 2.1.2, we tested more than one-hundred ^{3}MLCT guess structures, systematically varying the bond length of one py ligand (R_{py}) and of the bpy ligand in *trans* position to the former py (R_{bpy}) from the Ru-centre. Furthermore, the variation ranges of the time-dependent amplitudes $f^{PHP}(\tau)$ and $f^{3MLCT}(\tau)$ optimized in the fit were constrained according to the OTA results, achieving a remarkable stabilization of the fitting procedure. For a comprehensive description of the fitting details the reader can refer to the Supporting Information of ref. [113].

The results of OTA-assisted fitting of the transient EXAFS data are summarized in Fig. 6. The quality achieved in the reproduction of the experimental $\Delta\chi(q, \tau)$ can be noticed in Fig. 6a. Here, the best fit $\Delta\chi_{fit}(q, \tau)$ curves corresponding to the R-factor surface global minima are shown for each delay as black thick lines superimposed to the experimental spectra. Weighted PHP and ^{3}MLCT components are also reported. As an example, the contour plot of the fit R-factor as a function of the ^{3}MLCT structural parameters R_{bpy} and R_{py} optimized from the differential refinement of the $\Delta\chi_{exp}(q, 500\ ps)$ transient spectrum is shown in Fig. 6b.

The scenario resulting from TR-EXAFS analysis fairly confirmed the trends highlighted from DFT calculations, in agreement with the preliminary insights from TR-XSS discussed in Section 2.1.2 for the DFT-based ^{3}MLCT fingerprinting at τ = 100 ps. In particular, the structural minima found at τ = 500 and 3000 ps (estimated ^{3}MLCT population of 74% and 16%) consistently point out a R_{bpy} value of (2.03 ± 0.02) Å and a R_{py} bond length in the (2.16–2.20 ± 0.02) Å range (see Fig. 6c) for the ^{3}MLCT ES, with respect to the R_{py} = (2.09 ± 0.03) Å and R_{bpy} = (2.05 ± 0.02) Å values from EXAFS analysis of the GS structure (see Fig. 6d). Checking the optimized Ru–N(ligand) bond distances reported in Fig. 6c as a function of the time delay, it is however evident a discrepancy between the values observed at 150 ps and at the two subsequent time-points discussed so far. In particular, differential fitting of $\Delta\chi_{exp}(q, 150ps)$ yielded R_{bpy} and R_{py} bond lengths much closer to the GS values, which notably differ from the DFT values. Interestingly, the peculiarity of the 150 ps case can be related to an unaccounted structural contribution from the shorter-lived ^{3}MC ES, biasing the simplified 2-components fitting strategy employed. The presence of a ~ 3% ^{3}MC population at 150 ps, as estimated from OTA results (see Fig. 5b), is likely sufficient to significantly perturb the TR-EXAFS features due to the pronounced structural rearrangement expected in the anti-bounding state. Indeed, DFT analysis points out a 0.7 Å elongation of the R_{py} bond length in the ^{3}MC with respect to GS, together with significant distortions of the other Ru–N(ligands) bond distances and angle (see Fig. 6d). Unfortunately, the deconvolution of three independent components in the $\Delta\chi_{exp}(q, 150ps)$ spectrum was hampered by the limited signal-to-noise ratio of the collected data. Hence, the experimental elucidation of the ^{3}MC geometry, which is definitely the ramp towards the photochemical pathway, remains a challenging goal to be addressed in further studies, including a finer sampling and an enhanced collection statistics in the 50 ps−150 ps time-delay range, where a significant population of the short-lived ^{3}MC ES is expected.

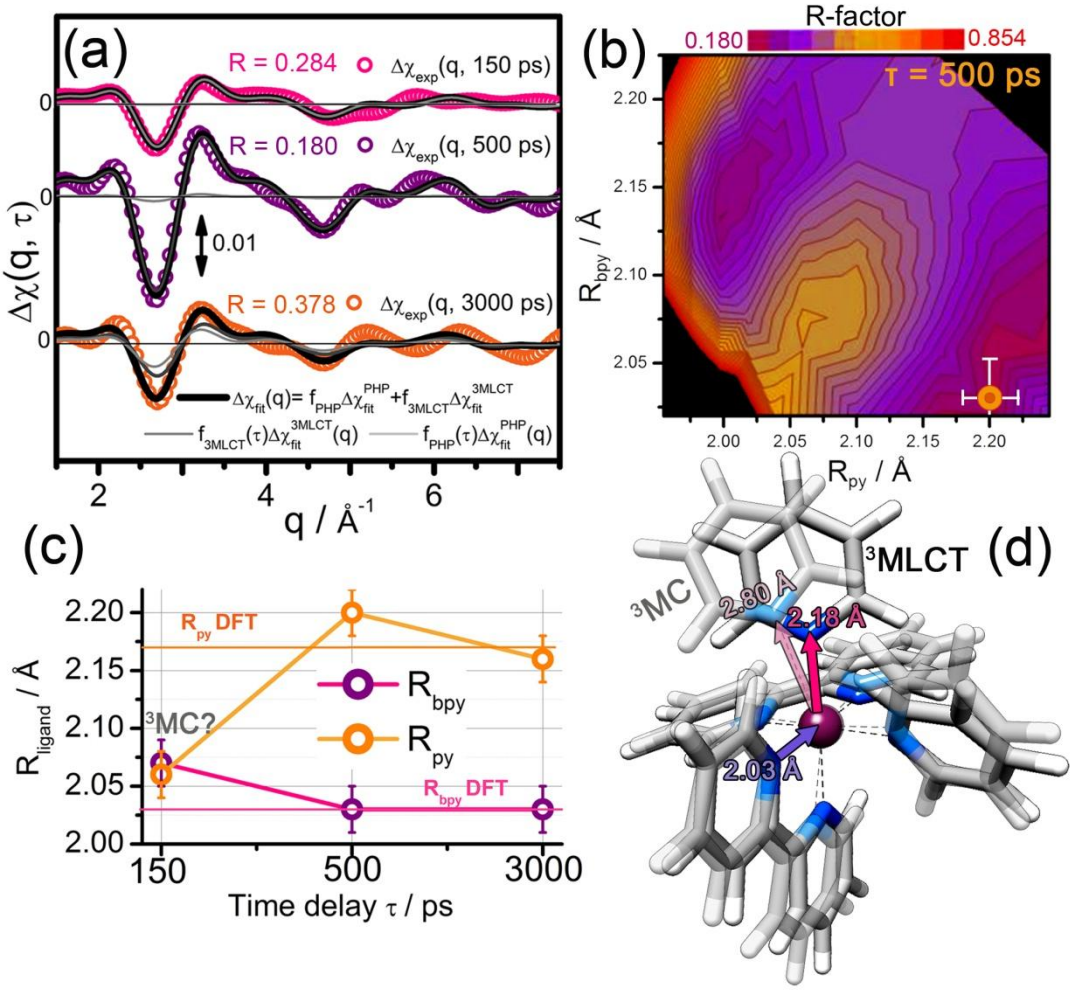

Fig. 6 Results from OTA-assisted differential fitting of the transient EXAFS data. (a) Best fit $\Delta\chi_{fit}(q,\tau)$ curves corresponding to the R-factor surface global minimum (black thick lines), superimposed to experimental TR-EXAFS data for τ = 150 (pink circles), 500(purple circles) and 3000 ps(orange circles); the fit components relative to the ^{3}MLCT and PHP contributions to the overall TR-EXAFS signal are indicated as dark and light grey thin lines, respectively. (b) Example of surface contour plot of the fit R-factor as a function of R_{bpy} and R_{py} bond distances obtained from the differential refinement of the $\Delta\chi_{exp}$(q, 500 ps) transient spectrum. The orange circle identifies the global minimum found in the R-factor values (R-factor = 0.180; R_{bpy} = (2.03 ± 0.02) Å; R_{py} = (2.20 ± 0.02) Å) while the experimental error interval (± 0.02 Å on both R_{bpy} and R_{py} axis, correspondent to the step between two adjacent point in the employed minimization grid) is marked by the white bars. It is worth noting the presence of an additional local minimum (R-factor = 0.194), likely due to an inversion in the shortening and lengthening of the R_{bpy} and R_{py}. (c) Time-evolution of the key-structural parameters optimized for the ^{3}MLCT ES of *cis*-$[Ru(bpy)_2(py)_2]^{2+}$, according to TR-EXAFS fitting results. (d) Superimposition of the ^{3}MLCT (full colour filling) and ^{3}MC (transparent colour filling) geometries. The major rearrangements with respect to GS are highlighted by coloured arrows, indicating the R_{bpy} and R_{py} values experimentally refined from the fitting of TR-EXAFS data. Unpublished Figure; parts (a) and (b) report data originally published in ref. [113].

2.3 The role of computational modelling in assisting ultrafast X-ray analysis

A close interplay between computational modelling and ultrafast X-ray experiments is necessary in the analysis of TR-XAS and TR-XSS data. The use of computational techniques is fundamental since they are able to provide excited state structures to be used as key initial guesses in the simulation of X-ray data. Without these starting points the structural information contained in the TR-X-ray data would be hardly interpreted. Moreover, computationally-obtained excited state structures are chemically more reliable than those obtained by random changes in bond and angles, particularly considering the level of sophistication reached by computational chemistry nowadays. Therefore, the support of computational modelling reduces the weight of the XAS and XSS signal simulation and prevents misinterpretation due to statistically

equivalent but chemically unequivalent cases (e.g. a monodentate pyridine ligand vs a pyridine ring of a bpy ligand).

Among the various computational methods available for the study of the electronic and structural properties of coordination complexes, DFT has been the most successful so far for its good performances on a variety of systems and for its relatively limited computational cost [143, 144]. Remarkably, DFT and TD-DFT have been successfully employed in the last decade to study the photophysics and photochemistry of complexes. In addition to their structural characterization capabilities (GS and ES geometries), they also allow to determine the energies and character of ES of different multiplicity and to evaluate their potential energy surfaces, which in combination with optical static and time-resolved techniques have often led to key developments [145-147].

Although DFT and TD-DFT remain the best choice for modelling inorganic and organometallic molecular systems, they suffer from limitations such as heavy parametrization and some unpredictability in their performance (benchmarking is highly recommended for such reason) [148]. Other ab initio methods (as for example the multi-configurational CASSCF, CASPT2) are becoming increasingly applicable to coordination compounds and other medium-to-large molecular systems, and are foreseen to overcome DFT issues in the description of Rydberg excited states, valence states of molecules with large π-systems [149-152], doubly excited states [153, 154], CT excited states [155-157], and conical intersections[158, 159].

3 Conclusions and perspectives

The *cis*-$[Ru(bpy)_2(py)_2]^{2+}$ case study reviewed in this contribution demonstrates how synchrotron ultrafast techniques can be employed to unravel the light-driven structural dynamics of photoactive transition metal complex in solution. The direct monitoring of the photoprocess involves several challenges, that we tackled developing an integrated multi-technique approach, mainly involving TR-XSS and TR-XAS synchrotron ultrafast techniques and computational modelling, supported by static XAS and OTA spectroscopies. In particular, TR-XSS allowed to detect the release of one pyridine ligand from the metal centre and the subsequent coordination of a water molecule within 800 ns from laser excitation. Furthermore TR-XAS provided information on the transient excited state geometries, showing that the ^{3}MLCT geometry is characterized by an elongation of the Ru−N(py) bond relative to the dissociating ligand and a shortening of the Ru–N(bpy) in trans to it. Analysis of 100 ps-resolution TR-XSS data confirmed the picture emerging from TR-XAS and OTA in terms of ESs dynamics and highlighted that photosubstitution occurs within 5 ns from laser excitation.

The impressive progresses in the field of synchrotron ultrafast characterization in the last two decades have allowed an unprecedented molecular-level understanding of photoinduced structural dynamics. These instruments can be employed, in some favourable cases, to film a photoactive metal complex “in action”, while rearranging after ultrafast laser excitation. This information uniquely allows to unravel the photoreaction mechanisms, monitoring both the local environment of the active site and the rich interactions between the excited solutes and the solvent environment. The recent efforts to improve the time-resolution achieved at third generation synchrotrons together with the XFELs breakthrough are paving the way to an unprecedented understanding of elementary mechanisms beneath photoreactions [85, 160]. The ultra high fluxes up to about 10^{12} photons per pulse (compared to 10^6 photons per pulse of present III generation synchrotrons) and extreme short length (tens of femtosecond, compared to hundreds of picosecond) will provide unique new opportunities, which are currently hard to imagine.

Nevertheless, X-ray ultrafast techniques are very demanding on the instrumental ground, as demonstrated by the small number of dedicated beamlines worldwide, and by the restricted access to users. Statistically-significant detection of the transient signals requires the highest source stability, an exceptional control of the acquisition condition and extremely sensitive detection schemes. In addition, the data treatment and modelling procedures required to reliably refine transient geometries are often highly requiring, in terms of time, computational resources and manpower.

Optical and vibrational transient spectroscopies are overall more accessible methods and allow to monitor the reaction dynamics in a quicker and less modelling-depended way with respect to X-ray methods. Optical/IR transient spectroscopies however lack in direct structural sensitivity: detailed kinetic information can be extracted from the transient spectral signatures, but the ES geometries can be only inferred in an indirect way, on the bases of existing knowledge of the investigated system. In addition, specific limitations affect the application of OTA to photoactive metal complexes [85]. For instance, the spectral fingerprints of the active transition metal centres are often overshadowed by the more intense $\pi \rightarrow \pi^*$ transitions of aromatic ligands. In addition, the MC states, which play a key role in photochemical processes, may be optically dark, or display absorption bands hardly distinguishable from those relative to other oxidation states of the metal. It is finally worth to note how IR transient spectroscopy of transition metal complexes mainly probes the time evolution of the vibration frequencies of specific functional group (*e.g.* carbonyls) coordinated to the metal centre. Hence, the technique applicability depends on the presence of suitable ligands, and the information derived on the metal centres is largely indirect.

Thus, ultrafast X-ray techniques and optical/vibrational transient spectroscopies are highly complementary strategies, each showing specific advantages and disadvantages when applied to investigate photoactive metal complexes. The need for a multitechnique approach is even more compelling when, for instance, applications to real photocatalysis are envisaged. Here, the multiplication of coexisting intermediate species and reaction pathways and the structural complexity which is often associated to the highest catalytic activity are serious challenges for ultrafast structural characterization.

Undoubtedly, most of the molecules investigated so far by TR-XSS and TR-XAS are, as *cis*-$[Ru(bpy)_2(py)_2]^{2+}$, model compounds, miming in a simplified way the functions of real catalytically or biologically-active systems. Nevertheless, few very recent studies are starting to face these difficulties, focusing on more complex (and catalytically relevant) molecular architectures. For instance, the $Ru_3(CO)_{12}$ photocatalyst is among the most complicated systems investigated by TR-XSS: Kong *et al.* [87, 88] considered so much as 16 possible intermediate structure to fully interpret the experimental data. In addition, Canton *et al.* [161] employed TR-XAS to monitor the electronic and nuclear modifications triggered by light induced electron-transfer in the $[(bpy)_2Ru^{II}(tpphz)^1Co^{III}(bpy)_2](PF_6)_5$ bimetallic complex (tpphz = tetrapyrido phenazine), representative of molecular photocatalysts employed in water splitting schemes. TR-XAS analysis, directly demonstrated that the photo-generated MLCT state of the Ru(II) unit acts as electron donor to the covalently bonded Co(III) moiety, which is reduced and undergoes an average bond elongation of 0.20 ± 0.03 Å, concomitantly to a spin flip. Another exciting application focused on the highly reactive Ir(IV) state of the Ir(III)-based water oxidation catalyst $Cp^*Ir(ppy)Cl$ (ppy = 2-phenylpyridine), captured by Vagnini *et al.* [162] by Ir LIII-edge TR-XAS at the, upon incorporation of in a covalent electron acceptor-chromophore-Ir complex triad. In both these studies, X-rays methods were accompanied by DFT-based modelling and OTA characterization.

Although still at the model compound level, these works represent the next step towards the characterization of real working photo-catalysts on the ultrafast scale, which is expected in the close future to foster the development of novel light-activated molecular devices with improved activity and selectivity.

Abbreviations

APS, Advanced Photon Source;
DFT, Density functional theory;
DW, Debye-Waller;
ES, Excited state;
ESRF, European Synchrotron Radiation Facility;
EXAFS, Extended X-ray absorption fine structure;
GS, Ground state;
MC, Metal centred (excited state);
MLCT, Metal to ligand charge transfer (excited state);

OTA, Optical transient absorption;
PMT, photomultiplier tubes;
TD-DFT, Time-dependent density functional theory
TR-XSS, Time-resolved X-ray solution scattering;
TR-XAS, Time-resolved X-ray absorption spectroscopy;
XAS, X-ray absorption spectroscopy;
XSS, X-ray solution scattering;

References

[1] B. Oregan, M. Gratzel, Nature 353 (1991) 737-740.
[2] M. Grätzel, Nature 414 (2001) 338-344.
[3] M. Grätzel, Inorg. Chem. 44 (2005) 6841-6851.
[4] R.E. Mahnken, M.A. Billadeau, E.P. Nikonowicz, H. Morrison, J. Am. Chem. Soc. 114 (1992) 9253-9265.
[5] K. Szacilowski, W. Macyk, A. Drzewiecka-Matuszek, M. Brindell, G. Stochel, Chem. Rev. 105 (2005) 2647-2694.
[6] D.A. Lutterman, P.K.L. Fu, C. Turro, J. Am. Chem. Soc. 128 (2006) 738-739.
[7] S.W. Magennis, A. Habtemariam, O. Novakova, J.B. Henry, S. Meier, S. Parsons, I.D.H. Oswald, V. Brabec, P.J. Sadler, Inorg. Chem. 46 (2007) 5059-5068.
[8] F.S. Mackay, J.A. Woods, P. Heringova, J. Kasparkova, A.M. Pizarro, S.A. Moggach, S. Parsons, V. Brabec, P.J. Sadler, Proc. Natl. Acad. Sci. U. S. A. 104 (2007) 20743-20748.
[9] F.S. Mackay, N.J. Farrer, L. Salassa, H.C. Tai, R.J. Deeth, S.A. Moggach, P.A. Wood, S. Parsons, P.J. Sadler, Dalton Trans. (2009) 2315-2325.
[10] J.D. Aguirre, A.M. Angeles-Boza, A. Chouai, J.P. Pellois, C. Turro, K.R. Dunbar, J. Am. Chem. Soc. 131 (2009) 11353-11360.
[11] N.J. Farrer, L. Salassa, P.J. Sadler, Dalton Trans. (2009) 10690-10701.
[12] S. Betanzos-Lara, L. Salassa, A. Habtemariam, P.J. Sadler, Chem. Commun. (2009) 6622-6624.
[13] S. Betanzos-Lara, L. Salassa, A. Habtemariam, O. Novakova, A.M. Pizarro, G.J. Clarkson, B. Liskova, V. Brabec, P.J. Sadler, Organometallics 31 (2012) 3466-3479.
[14] A.D. Ostrowski, P.C. Ford, Dalton Trans. (2009) 10660-10669.
[15] R. Alberto, R. Motterlini, Dalton Trans. (2007) 1651-1660.
[16] U. Schatzschneider, Eur. J. Inorg. Chem. (2010) 1451-1467.
[17] L. Zayat, C. Calero, P. Albores, L. Baraldo, R. Etchenique, J. Am. Chem. Soc. 125 (2003) 882-883.
[18] V. Fernandez-Moreira, F.L. Thorp-Greenwood, M.P. Coogan, Chem. Comm. 46 (2010) 186-202.
[19] M.R. Gill, H. Derrat, C.G.W. Smythe, G. Battaglia, J.A. Thomas, ChemBioChem 12 (2011) 877-880.
[20] V. Balzani, Photochem. Photobiol. Sci. 2 (2003) 459-476.
[21] V. Balzani, A. Credi, M. Venturi, Chem. Soc. Rev. 38 (2009) 1542-1550.
[22] H. Yersin, Highly Efficient OLEDs with Phosphorescent Materials, Wiley-VCH, Weinheim, 2008.
[23] C. Ulbricht, B. Beyer, C. Friebe, A. Winter, U.S. Schubert, Adv. Mater. 21 (2009) 4418-4441.
[24] Y. Chi, P.T. Chou, Chem. Soc. Rev. 39 (2010) 638-655.
[25] P.T. Chou, Y. Chi, Chem.-Eur. J. 13 (2007) 380-395.
[26] A. Ruggi, F.W.B. van Leeuwen, A.H. Velders, Coord. Chem. Rev. 255 (2011) 2542-2554.
[27] N. Hoffmann, ChemSusChem 5 (2012) 352-371.
[28] A. Inagaki, M. Akita, Coord. Chem. Rev. 254 (2010) 1220-1239.
[29] V. Artero, M. Chavarot-Kerlidou, M. Fontecave, Angew. Chem.-Int. Edit. 50 (2011) 7238-7266.
[30] A.J. Morris, G.J. Meyer, E. Fujita, Accounts Chem. Res. 42 (2009) 1983-1994.
[31] C.D. Windle, R.N. Perutz, Coord. Chem. Rev. 256 (2012) 2562-2570.
[32] M. Dantus, M.J. Rosker, A.H. Zewail, J. Chem. Phys. 87 (1987) 2395-2397.
[33] T.S. Rose, M.J. Rosker, A.H. Zewail, J. Chem. Phys. 88 (1988) 6672-6673.
[34] A.H. Zewail, Science 242 (1988) 1645-1653.
[35] A.H. Zewail, J. Phys. Chem. A 104 (2000) 5660-5694.
[36] A.H. Zewail, Angew. Chem.-Int. Edit. 39 (2000) 2587-2631.
[37] C.V. Shank, Science 233 (1986) 1276-1280.
[38] A.H. Zewail, Ultrafast Dynamics of The Chemical Bond, Word Scientific, Singapore, 1994.

[39] E. Lenderink, K. Duppen, D.A. Wiersma, J. Phys. Chem. 99 (1995) 8972-8977.
[40] M. Chachisvilis, H. Fidder, V. Sundstrom, Chem. Phys. Lett. 234 (1995) 141-150.
[41] P.K. Walhout, J.C. Alfano, Y. Kimura, C. Silva, P.J. Reid, P.F. Barbara, Chem. Phys. Lett. 232 (1995) 135-140.
[42] R.M. Whitnell, K.R. Wilson, Y.J. Yan, A.H. Zewail, J. Mol. Liq. 61 (1994) 153-165.
[43] Y.J. Yan, L.E. Fried, S. Mukamel, J. Phys. Chem. 93 (1989) 8149-8162.
[44] G.R. Fleming, Chemical Applications of Ultrafast Spectroscopy, Oxford University Press, Oxford, UK, 1986.
[45] L.X. Chen, Angew. Chem.-Int. Edit. 43 (2004) 2886-2905.
[46] C. Rulliere, Femtosecond Laser Pulses: Principles and Experiments, Springer, New York, 2004.
[47] A. Weiner, Ultrafast Optics, Wiley, Hoboken, New Jersey, 2011.
[48] M. Andersson, J. Davidsson, L. Hammarstrom, J. Korppi-Tommola, T. Peltola, J. Phys. Chem. B 103 (1999) 3258-3262.
[49] S. Ramakrishna, F. Willig, J. Phys. Chem. B 104 (2000) 68-77.
[50] J.P. Wang, S. Link, C.D. Heyes, M.A. El-Sayed, Biophys. J. 83 (2002) 1557-1566.
[51] N. Ismail, L. Blancafort, M. Olivucci, B. Kohler, M.A. Robb, J. Am. Chem. Soc. 124 (2002) 6818-6819.
[52] J.K. McCusker, Accounts Chem. Res. 36 (2003) 876-887.
[53] L.X. Chen, G.B. Shaw, I. Novozhilova, T. Liu, G. Jennings, K. Attenkofer, G.J. Meyer, P. Coppens, J. Am. Chem. Soc. 125 (2003) 7022-7034.
[54] L. Dhar, J.A. Rogers, K.A. Nelson, Chem. Rev. 94 (1994) 157-193.
[55] J.R. Schoonover, C.A. Bignozzi, T.J. Meyer, Coord. Chem. Rev. 165 (1997) 239-266.
[56] J.R. Schoonover, G.F. Strouse, Chem. Rev. 98 (1998) 1335-1355.
[57] C. Kotting, K. Gerwert, ChemPhysChem 6 (2005) 881-888.
[58] D.S. Larsen, R. van Grondelle, ChemPhysChem 6 (2005) 828-837.
[59] E.T.J. Nibbering, H. Fidder, E. Pines, Ultrafast chemistry: Using time-resolved vibrational spectroscopy for interrogation of structural dynamics, Annual Review of Physical Chemistry, Annual Reviews, Palo Alto, 2005, pp. 337-367.
[60] J.M. Butler, M.W. George, J.R. Schoonover, D.M. Dattelbaum, T.J. Meyer, Coord. Chem. Rev. 251 (2007) 492-514.
[61] M. Banno, K. Ohta, S. Yamaguchi, S. Hirai, K. Tominaga, Accounts Chem. Res. 42 (2009) 1259-1269.
[62] B.J. Siwick, J.R. Dwyer, R.E. Jordan, R.J.D. Miller, Science 302 (2003) 1382-1385.
[63] C.Y. Ruan, F. Vigliotti, V.A. Lobastov, S.Y. Chen, A.H. Zewail, Proc. Natl. Acad. Sci. U. S. A. 101 (2004) 1123-1128.
[64] S. Chen, M.T. Seidel, A.H. Zewail, Proc. Natl. Acad. Sci U.S.A. 102 (2005) 8854-8859.
[65] R. Srinivasan, J.S. Feenstra, S.T. Park, S.J. Xu, A.H. Zewail, Science 307 (2005) 558-563.
[66] A.H. Zewail, J.M. Thomas, 4D Electron Microscopy: Imaging in Space and Time, Imperial College Press, Singapore, 2010.
[67] C. Bressler, M. Chergui, Chem. Rev. 104 (2004) 1781-1812.
[68] H. Ihee, Acc. Chem. Res. 42 (2009) 356-366.
[69] T.K. Kim, J.H. Lee, M. Wulff, Q.Y. Kong, H. Ihee, ChemPhysChem 10 (2009) 1958-1980.
[70] C. Lamberti, Surf. Sci. Rep. 53 (2004) 1-197.
[71] S. Bordiga, E. Groppo, G. Agostini, J.A. van Bokhoven, C. Lamberti, Chem. Rev. 113 (2013) 1736-1850.
[72] L. Mino, G. Agostini, E. Borfecchia, D. Gianolio, A. Piovano, E. Gallo, C. Lamberti, J. Phys. D-Appl. Phys. 46 (2013).
[73] E. Borfecchia, C. Garino, L. Salassa, C. Lamberti, Philos. Trans. R. Soc. A-Math. Phys. Eng. Sci. 371 (2013) 20120132.
[74] M. Chergui, A.H. Zewail, ChemPhysChem 10 (2009) 28-43.
[75] M. Abo-Bakr, J. Feikes, K. Holldack, G. Wustefeld, H.W. Hubers, Phys. Rev. Lett. 88 (2002).
[76] I. Radu, C. Stamm, N. Pontius, T. Kachel, P. Ramm, J.U. Thiele, H.A. Durr, C.H. Back, Phys. Rev. B 81 (2010).
[77] S. Ibrahimkutty, D. Issenmann, S. Schleef, A.S. Muller, Y.L. Mathis, B. Gasharova, E. Huttel, R. Steininger, J. Gottlicher, T. Baumbach, A. Bartels, C. Janke, A. Plech, J. Synchrot. Radiat. 18 (2011) 539-545.

[78] H. Navirian, R. Shayduk, W. Leitenberger, J. Goldshteyn, P. Gaal, M. Bargheer, Rev. Sci. Instrum. 83 (2012).
[79] H. Wiedemann, Particle Accelerator Physics, Springer-Verlag Berlin, 1999, pp. 211-242.
[80] X. Wang, S.Q. Tian, G.M. Liu, Nucl. Sci. Tech. 21 (2010) 134-140.
[81] R.W. Schoenlein, S. Chattopadhyay, H.H.W. Chong, T.E. Glover, P.A. Heimann, C.V. Shank, A.A. Zholents, M.S. Zolotorev, Science 287 (2000) 2237-2240.
[82] S. Khan, K. Holldack, T. Kachel, R. Mitzner, T. Quast, Phys. Rev. Lett. 97 (2006).
[83] P. Beaud, S.L. Johnson, A. Streun, R. Abela, D. Abramsohn, D. Grolimund, F. Krasniqi, T. Schmidt, V. Schlott, G. Ingold, Phys. Rev. Lett. 99 (2007).
[84] C. Bressler, C. Milne, V.T. Pham, A. ElNahhas, R.M. van der Veen, W. Gawelda, S. Johnson, P. Beaud, D. Grolimund, M. Kaiser, C.N. Borca, G. Ingold, R. Abela, M. Chergui, Science 323 (2009) 489-492.
[85] L.X. Chen, X. Zhang, J. Phys. Chem. Lett. (2013) 4000-4013.
[86] M. Christensen, K. Haldrup, K. Bechgaard, R. Feidenhans'l, Q.Y. Kong, M. Cammarata, M. Lo Russo, M. Wulff, N. Harrit, M.M. Nielsen, J. Am, T.K. Kim, J.H. Lee, M. Wulff, Q. Kong, H. Ihee, ChemPhysChem 10 (2009) 3140-3140.
[87] Q.Y. Kong, J.H. Lee, A. Plech, M. Wulff, H. Ihee, M.H.J. Koch, Angew. Chem.-Int. Edit. 47 (2008) 5550-5553.
[88] Q. Kong, J.H. Lee, K.H. Kim, J. Kim, M. Wulff, H. Ihee, M.H.J. Koch, J. Am. Chem. Soc. 132 (2010) 2600-2607.
[89] J.G. Bentsen, M.S. Wrighton, J. Am. Chem. Soc. 109 (1987) 4518-4530.
[90] B.F.G. Johnson, J. Lewis, M.V. Twigg, J. Organomet. Chem. 67 (1974) C75-C76.
[91] M. Christensen, K. Haldrup, K. Bechgaard, R. Feidenhans'l, Q.Y. Kong, M. Cammarata, M. Lo Russo, M. Wulff, N. Harrit, M.M. Nielsen, J. Am. Chem. Soc. 131 (2009) 502-508.
[92] K. Haldrup, T. Harlang, M. Christensen, A. Dohn, T.B. van Driel, K.S. Kjaer, N. Harrit, J. Vibenholt, L. Guerin, M. Wulff, M.M. Nielsen, Inorg. Chem. 50 (2011) 9329-9336.
[93] A.P. Zipp, Coord. Chem. Rev. 84 (1988) 47-83.
[94] D.M. Roundhill, H.B. Gray, C.M. Che, Acc. Chem. Res. 22 (1989) 55-61.
[95] D.C. Smith, H.B. Gray, Coord. Chem. Rev. 100 (1990) 169-181.
[96] L.X. Chen, X.Y. Zhang, E.C. Wasinger, K. Attenkofer, G. Jennings, A.Z. Muresan, J.S. Lindsey, J. Am. Chem. Soc. 129 (2007) 9616-9618.
[97] L.X. Chen, X.Y. Zhang, E.C. Wasinger, J.V. Lockard, A.B. Stickrath, M.W. Mara, K. Attenkofer, G. Jennings, G. Smolentsev, A. Soldatov, Chem. Sci. 1 (2010) 642-650.
[98] L.X. Chen, G. Jennings, T. Liu, D.J. Gosztola, J.P. Hessler, D.V. Scaltrito, G.J. Meyer, J. Am. Chem. Soc. 124 (2002) 10861-10867.
[99] G.B. Shaw, C.D. Grant, H. Shirota, E.W. Castner, G.J. Meyer, L.X. Chen, J. Am. Chem. Soc. 129 (2007) 2147-2160.
[100] M. Saes, C. Bressler, R. Abela, D. Grolimund, S.L. Johnson, P.A. Heimann, M. Chergui, Phys. Rev. Lett. 90 (2003).
[101] W. Gawelda, M. Johnson, F.M.F. de Groot, R. Abela, C. Bressler, M. Chergui, J. Am. Chem. Soc. 128 (2006) 5001-5009.
[102] A. El Nahhas, R.M. van der Veen, T.J. Penfold, V.T. Pham, F.A. Lima, R. Abela, A.M. Blanco-Rodriguez, S. Zalis, A. Vlcek, I. Tavernelli, U. Rothlisberger, C.J. Milne, M. Chergui, J. Phys. Chem. A 117 (2013) 361-369.
[103] R.M. van der Veen, C.J. Milne, A. El Nahhas, F.A. Lima, V.T. Pham, J. Best, J.A. Weinstein, C.N. Borca, R. Abela, C. Bressler, M. Chergui, Angew. Chem.-Int. Edit. 48 (2009) 2711-2714.
[104] J.V. Lockard, A.A. Rachford, G. Smolentsev, A.B. Stickrath, X.H. Wang, X.Y. Zhang, K. Atenkoffer, G. Jennings, A. Soldatov, A.L. Rheingold, F.N. Castellano, L.X. Chen, J. Phys. Chem. A 114 (2010) 12780-12787.
[105] M.R. Harpham, S.C. Nguyen, Z.R. Hou, J.C. Grossman, C.B. Harris, M.W. Mara, A.B. Stickrath, Y. Kanai, A.M. Kolpak, D. Lee, D.J. Liu, J.P. Lomont, K. Moth-Poulsen, N. Vinokurov, L.X. Chen, K.P.C. Vollhardt, Angew. Chem.-Int. Edit. 51 (2012) 7692-7696.
[106] M.R. Harpham, A.B. Stickrath, X. Zhang, J. Huang, M.W. Mara, L.X. Chen, D.-J. Liu, J. Phys. Chem. A 117 (2013) 9807-9813.
[107] M. Khalil, M.A. Marcus, A.L. Smeigh, J.K. McCusker, H.H.W. Chong, R.W. Schoenlein, J. Phys. Chem. A 110 (2006) 38-44.

[108] W. Gawelda, A. Cannizzo, V.T. Pham, A. El Nahhas, C.J. Milne, R. van der Veen, C. Bressler, M. Chergui, Chimia 61 (2007) 179-183.
[109] N. Huse, T.K. Kim, L. Jamula, J.K. McCusker, F.M.F. de Groot, R.W. Schoenlein, J. Am. Chem. Soc. 132 (2010) 6809-6816.
[110] A. Cannizzo, C.J. Milne, C. Consani, W. Gawelda, C. Bressler, F. van Mourik, M. Chergui, Coord. Chem. Rev. 254 (2010) 2677-2686.
[111] K. Haldrup, G. Vanko, W. Gawelda, A. Galler, G. Doumy, A.M. March, E.P. Kanter, A. Bordage, A. Dohn, T.B. van Driel, K.S. Kjaer, H.T. Lemke, S.E. Canton, J. Uhlig, V. Sundstrom, L. Young, S.H. Southworth, M.M. Nielsen, C. Bressler, J. Phys. Chem. A 116 (2012) 9878-9887.
[112] L. Salassa, E. Borfecchia, T. Ruiu, C. Garino, D. Gianolio, R. Gobetto, P.J. Sadler, M. Cammarata, M. Wulff, C. Lamberti, Inorg. Chem. 49 (2010) 11240-11248.
[113] E. Borfecchia, C. Garino, L. Salassa, T. Ruiu, D. Gianolio, X. Zhang, K. Attenkofer, L.X. Chen, R. Gobetto, P.J. Sadler, C. Lamberti, Dalton Trans. 42 (2013) 6564-6571.
[114] B. Durham, J.V. Caspar, J.K. Nagle, T.J. Meyer, J. Am. Chem. Soc. 104 (1982) 4803-4810.
[115] J.V. Caspar, T.J. Meyer, Inorg. Chem. 22 (1983) 2444-2453.
[116] W.M. Wacholtz, R.A. Auerbach, R.H. Schmehl, M. Ollino, W.R. Cherry, Inorg. Chem. 24 (1985) 1758-1760.
[117] M. Adelt, M. Devenney, T.J. Meyer, D.W. Thompson, J.A. Treadway, Inorg. Chem. 37 (1998) 2616-2617.
[118] D.W. Thompson, C.N. Fleming, B.D. Myron, T.J. Meyer, J. Phys. Chem. B 111 (2007) 6930-6941.
[119] P.S. Wagenknecht, P.C. Ford, Coord. Chem. Rev. 255 (2011) 591-616.
[120] Q. Sun, S. Mosquera-Vazquez, L.M. Lawson Daku, L. Guénée, H.A. Goodwin, E. Vauthey, A. Hauser, J. Am. Chem. Soc. 135 (2013) 13660-13663.
[121] L. Salassa, C. Garino, G. Salassa, R. Gobetto, C. Nervi, J. Am. Chem. Soc. 130 (2008) 9590-9597.
[122] L. Salassa, D. Gianolio, C. Garino, G. Salassa, E. Borfecchia, T. Ruiu, C. Nervi, R. Gobetto, R. Bizzarri, P.J. Sadler, C. Lamberti, J. Phys.: Conf. Series 190 (2009) 012141.
[123] M. Wulff, A. Plech, L. Eybert, R. Randler, F. Schotte, P. Anfinrud, Faraday Discuss. 122 (2002) 13-26.
[124] A.L. Harris, J.K. Brown, C.B. Harris, Ann. Rev. Phys. Chem. 39 (1988) 341-366.
[125] M. Cammarata, M. Lorenc, T.K. Kim, J.H. Lee, Q.Y. Kong, E. Pontecorvo, M. Lo Russo, G. Schiro, A. Cupane, M. Wulff, H. Ihee, J. Chem. Phys. 124 (2006) 124504.
[126] H. Ihee, M. Wulff, J. Kim, S. Adachi, Int. Rev. Phys. Chem. 29 (2010) 453-520.
[127] A. Plech, M. Wulff, S. Bratos, F. Mirloup, R. Vuilleumier, F. Schotte, P.A. Anfinrud, Phys. Rev. Lett. 92 (2004) 125505.
[128] M. Wulff, S. Bratos, A. Plech, R. Vuilleumier, F. Mirloup, M. Lorenc, Q. Kong, H. Ihee, J. Chem. Phys. 124 (2006) 034501.
[129] J. Davidsson, J. Poulsen, M. Cammarata, P. Georgiou, R. Wouts, G. Katona, F. Jacobson, A. Plech, M. Wulff, G. Nyman, R. Neutze, Phys. Rev. Lett. 94 (2005) 245503.
[130] J.H. Lee, K.H. Kim, T.K. Kim, Y. Lee, H. Ihee, J. Chem. Phys. 125 (2006) 174504
[131] D. Gianolio, E. Borfecchia, C. Garino, T. Ruiu, C. Lamberti, L. Salassa, J. Phys.: Conf. Ser. 430 (2013) 012125.
[132] D.V. Pinnick, B. Durham, Inorg. Chem. 23 (1984) 1440-1445.
[133] P. Debye, Ann. der Physik 46 (1915) 809-823.
[134] A. Guinier, X-ray Diffraction, Dover, New York, US, 1963.
[135] B.E. Warren, X-ray Diffraction, Dover, New York, 1969.
[136] C. Bressler, M. Chergui, Annu. Rev. Phys. Chem. 61 (2010) 263-282.
[137] L.X. Chen, W.J.H. Jager, G. Jennings, D.J. Gosztola, A. Munkholm, J.P. Hessler, Science 292 (2001) 262-264.
[138] G. Jennings, W.J.H. Jager, L.X. Chen, Rev. Sci. Instrum. 73 (2002) 362-368.
[139] L.X. Chen, G.B. Shaw, T. Liu, G. Jennings, K. Attenkofer, Phys. Scr. T115 (2005) 93-96.
[140] X.Y. Zhang, G. Smolentsev, J.C. Guo, K. Attenkofer, C. Kurtz, G. Jennings, J.V. Lockard, A.B. Stickrath, L.X. Chen, J. Phys. Chem. Lett. 2 (2011) 628-632.
[141] S. Wallin, J. Davidsson, J. Modin, L. Hammarstrom, J. Phys. Chem. A 109 (2005) 4697-4704.
[142] Y. Liu, D.B. Turner, T.N. Singh, A.M. Angeles-Boza, A. Chouai, K.R. Dunbar, C. Turro, J. Am. Chem. Soc. 131 (2008) 26-27.
[143] L. Gonzalez, D. Escudero, L. Serrano-Andres, ChemPhysChem 13 (2012) 28-51.

[144] A. Dreuw, M. Head-Gordon, Chem. Rev. 105 (2005) 4009-4037.
[145] C.J. Cramer, D.G. Truhlar, Phys. Chem. Chem. Phys. 11 (2009) 10757-10816.
[146] C. Garino, L. Salassa, Philos. Trans. R. Soc. A-Math. Phys. Eng. Sci. 371 (2013).
[147] A. Vlcek, S. Zalis, Coord. Chem. Rev. 251 (2007) 258-287.
[148] D. Jacquemin, E. Bremond, A. Planchat, I. Ciofini, C. Adamo, J. Chem. Theory Comput. 7 (2011) 1882-1892.
[149] Z.L. Cai, K. Sendt, J.R. Reimers, J. Chem. Phys. 117 (2002) 5543-5549.
[150] S. Grimme, M. Parac, ChemPhysChem 4 (2003) 292-+.
[151] M. Parac, S. Grimme, Chem. Phys. 292 (2003) 11-21.
[152] M. Wanko, M. Garavelli, F. Bernardi, T.A. Niehaus, T. Frauenheim, M. Elstner, J. Chem. Phys. 120 (2004) 1674-1692.
[153] R.J. Cave, F. Zhang, N.T. Maitra, K. Burke, Chem. Phys. Lett. 389 (2004) 39-42.
[154] N.T. Maitra, F. Zhang, R.J. Cave, K. Burke, J. Chem. Phys. 120 (2004) 5932-5937.
[155] A. Dreuw, M. Head-Gordon, J. Am. Chem. Soc. 126 (2004) 4007-4016.
[156] A. Dreuw, J.L. Weisman, M. Head-Gordon, J. Chem. Phys. 119 (2003) 2943-2946.
[157] M. Parac, S. Grimme, J. Phys. Chem. A 106 (2002) 6844-6850.
[158] B.G. Levine, C. Ko, J. Quenneville, T.J. Martinez, Mol. Phys. 104 (2006) 1039-1051.
[159] L. Serrano-Andres, M. Merchan, R. Lindh, J. Chem. Phys. 122 (2005).
[160] H.T. Lemke, C. Bressler, L.X. Chen, D.M. Fritz, K.J. Gaffney, A. Galler, W. Gawelda, K. Haldrup, R.W. Hartsock, H. Ihee, J. Kim, K.H. Kim, J.H. Lee, M.M. Nielsen, A.B. Stickrath, W.K. Zhang, D.L. Zhu, M. Cammarata, J. Phys. Chem. A 117 (2013) 735-740.
[161] S.E. Canton, X.Y. Zhang, J.X. Zhang, T.B. van Driel, K.S. Kjaer, K. Haldrup, P. Chabera, T. Harlang, K. Suarez-Alcantara, Y.Z. Liu, J. Perez, A. Bordage, M. Papai, G. Vanko, G. Jennings, C.A. Kurtz, M. Rovezzi, P. Glatzel, G. Smolentsev, J. Uhlig, A.O. Dohn, M. Christensen, A. Galler, W. Gawelda, C. Bressler, H.T. Lemke, K.B. Moller, M.M. Nielsen, R. Lomoth, K. Warnmark, V. Sundstrom, J. Phys. Chem. Lett. 4 (2013) 1972-1976.
[162] M.T. Vagnini, M.W. Mara, M.R. Harpham, J. Huang, M.L. Shelby, L.X. Chen, M.R. Wasielewski, Chem. Sci. 4 (2013) 3863-3873.